Solar Energy 273 (2024) 112546

Contents lists available at ScienceDirect

Solar Energy

journal homepage: www.elsevier.com/locate/solener

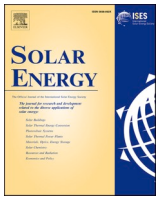

Modelling reflection in the centrifugal solar particle receiver

Serdar Hicdurmaz [a,b,*], Johannes Grobbel [c], Reiner Buck [a], Bernhard Hoffschmidt [b,d]

[a] German Aerospace Center (DLR), Institute of Solar Research, Stuttgart 70569, Germany
[b] Chair of Solar Components, RWTH Aachen University, Aachen 52056, Germany
[c] German Aerospace Center (DLR), Institute of Future Fuels 52428 Jülich, Germany
[d] German Aerospace Center (DLR), Institute of Solar Research, Cologne 51147, Germany

ARTICLE INFO

Keywords:
Solar Particle Receivers
Ray Tracing
Radiation in Particle Beds
Bidirectional Reflectance Distribution Function (BRDF)

ABSTRACT

In this study, a novel reflection model for particle beds formed by diffuse, gray, opaque and spherical particles is developed, and applied to the Centrifugal Solar Particle Receiver (CentRec). The reflection from particle beds comprised of diffuse reflecting particles are neither diffuse nor specular but incidence angle dependent due to the spherical surface of the particles forming the particle bed. The reflection characteristics of a particle bed being representative for the CentRec application is derived for a wide range of incidence angles of the incoming rays ($0° \leq \gamma_{gen} \leq 85°$). Later, the derived characteristics are imported to the in-house ray tracing tool SPRAY. A realistic ray distribution is generated by taking the heliostat configuration into account. The absorbed power distribution on the particle film surface in the CentRec is found after several reflections inside the CentRec cavity. The model results are compared with resolved MCRT results for typical CentRec operating conditions. Very high accuracy in terms of reflection loss through the aperture and absorbed power distribution in the receiver is achieved with the developed reflection model. The required computational time to model the solar irradiation in the CentRec is reduced significantly and there is still room for improvement.

1. Introduction

Particle solar receivers using granular materials as heat transfer and storage medium have been considered as a new generation CSP solar tower technology for more than a decade [1–3]. Compared to molten salt-based solar towers, particle receivers promise higher thermal efficiency and lower operational and component cost. Various receiver designs in which particles are heated directly or indirectly with concentrated solar irradiation have been proposed in recent years [4–7]. Some concepts have already reached TRL of 5–7 in the way of commercialization of the technology. The demonstration scale (1–2 MW_{th}) solar towers on the top of which particle receivers are placed, are being built in several locations of the world as of 2023 to show functionality of sub-components of particle-based CSP systems [8].

The Centrifugal Particle Solar Receiver (CentRec) is one of the prominent particle receiver designs. It is a direct absorption receiver using ceramic particles as the heat transfer fluid. In the CentRec, the ceramic particles which are accelerated centrifugally and gravitationally, descend through an inclined rotating drum while being directly exposed to the solar irradiation through the aperture, as depicted in Fig. 1. Particles are accelerated to the tangential velocity of the rotating cavity thanks to the inlet distributor so that there is no relative tangential velocity between particles and the cavity when particles start to form a particle film on the cavity wall. In every rotation the particles experience a changing effective force from the combination of the changing centrifugal force and the constant gravitation force. This makes the particles slightly advance in axial direction in every turn, and eventually leave the receiver after a certain residence time. Compared to other particle receiver concepts, CentRec allows for an active adjustment of particle residence time and thus particle film conditions by adjusting the rotational speed of the drum. The direct heating and adjustable residence time allow a large temperature increase between inlet and outlet. The radiation shield, located on the facade of the particle collector ring, and the receiver aperture are designed to maximize the solar influx while minimizing the reflection and thermal emission losses. More details about design and operation of the CentRec can be found in [9]. Wu [6] demonstrated that an opaque particle film flowing on the receiver wall can be obtained for various combinations of the receiver (drum) rotational speed and the particle mass flow rate by employing a proof-of-concept scale receiver with 17 cm cavity diameter. For a mass flow rate of 8 g/s, being very low for the CentRec, and 670 kW/m^2 of mean heat flux at the aperture, thermal efficiencies up to 75 %

* Corresponding author at: German Aerospace Center (DLR), Institute of Solar Research, Stuttgart 70569, Germany (Serdar Hicdurmaz).
E-mail address: serdar.hicdurmaz@dlr.de (S. Hicdurmaz).

https://doi.org/10.1016/j.solener.2024.112546
Received 11 September 2023; Received in revised form 4 March 2024; Accepted 13 April 2024
Available online 18 April 2024

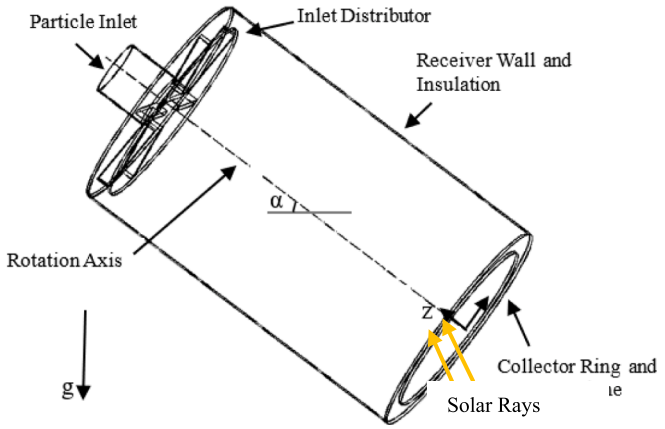

Fig. 1. Schematic view of the centrifugal receiver.

were achieved in a solar simulator. Note that the thermal power of this receiver is ~ 10 kW_{th} due to the small aperture diameter, being 0.138 m. For a fixed temperature difference between the inlet and outlet particles, the thermal power of the receiver is proportional to the particle mass flow rate. Ebert et al. [10] scaled up the design to ~ 1.5 m of cavity diameter and 3 kg/s of mass flow rate and tested the stability of the particle film by running cold particle tests. Amsbeck et al. [11] carried out first large scale hot tests with an 100 kW_{el} infrared heater and 0.4 kg/s of mass flow rate and proved scalability of the concept. Particle temperatures of up to 700 °C were achieved, limited by technical problems with the infrared heater. Finally, the CentRec has been demonstrated to reach a particle outlet temperature of 965 °C for a mass flow rate of 0.07 – 0.18 kg/s at the Solar Tower Jülich [12,13].

The thermal efficiency of the CentRec design is mainly limited by radiation and convection losses. The atmospheric air entering from the aperture plane and circulating through the cavity causes a "convection loss". Additionally, particles emit significant thermal radiation as they approach temperatures of ~ 1000 °C. A portion of these re-emissions are lost through the aperture, resulting in an "emission loss". The authors have shown that a radiation enclosure model with the assumption of a diffuse and gray particle film surface gives very similar results to resolved MCRT results for a particle emissivity being higher than 0.6 in terms of emission loss through the aperture [9]. Finally, a portion of concentrated solar irradiation is reflected from the receiver back to the ambient through the aperture due to non-black particles and cavity surfaces. This loss is denoted as "reflection loss". In most cases, the conduction loss through the insulation and other receiver components is negligibly small [14]. In this study, a particular interest is given to modeling the reflection loss.

Radiative heat transfer in a particulate medium can be calculated by employing the Radiative Transfer Equation (RTE) that accounts for absorption, scattering and emission within the medium [15]. Absorption and scattering of external beams in dilute [16] and dense [17] particle beds has been investigated experimentally and numerically. However, an analytical solution of the RTE is very challenging for complex domains, and simplifications based on certain assumptions are needed for the numerical solution depending on the complexity of the model. In radiation models developed for the falling particle receiver where the particulate medium is optically thin as opposed to the CentRec application, the discrete-ordinates (DO) approach that solves the RTE with a spatial and angular discretization has been employed to model scattering and absorption of the solar irradiation by applying a wavelength band of 0–4.5 μm [18,19]. However, in the current study, particles are handled as a discrete phase instead of a continuum phase where the DO approach is applicable. This is because particle interactions have significant effect on the particle film characteristics in densely moving beds, and needs to be accurately modeled with a discrete phase approach.

Reflection and absorption behavior of bulk granular material is also of great interest for several industries such as laser 3D printing [20,21]. In the laser additive manufacturing application, an external beam is also applied to dense metallic particles with certain incidence angle, which makes it very similar to the CentRec application in terms of absorption and reflection characteristics. Absorption, reflection and transmission behavior of various ordered and random packing structures of powder beds for this application type have been investigated theoretically and experimentally in several studies [22,23]. In a previous study, the authors formulated the radiation penetration behavior in randomly packed beds formed by diffuse, gray and spherical particles by accounting for particle absorptivity, bed porosity and incidence angle of the incoming rays. The developed radiation penetration model has also been applied to the CentRec [24]. However, the reflection from the particle film has not been investigated in detail yet. Note that thermal emission is not the scope of this study.

2. Model development

In order to model the thermal behavior of the CentRec, Discrete Element Method (DEM)-based heat transfer models have been preferred in previous studies [14,24,25]. When the relatively low thermal conductivity of the particle film comprised of the ceramic particles is considered, mixing of particles within the particle film has a significant effect on the thermal efficiency of the CentRec. To capture this effect and the particle interactions within the film, the open source DEM tool LIGGGHTS is utilized. Thus, the addressed reflection model needs to be DEM-compatible.

Monte Carlo ray tracing (MCRT) is a reliable, simple and accurate approach to find how solar irradiation is distributed to the particles; however, it suffers from the increasing computational burden as the number of particles increases in the simulation. A radiation penetration model developed previously by the authors can predict the energy distribution in a particulate domain without running a ray tracing simulation as long as the irradiation and incidence angle distribution on the particle film are provided, as shown in a previous study [24]. However, the reflection from a particle bed was not investigated in that study. Thus, a complementary reflection model is addressed in this work to find how the solar irradiation is distributed to the particle film surface after several reflections in the receiver cavity. Note that both studies assume spherical, diffuse, gray and opaque particles. It is also assumed that there is no refraction or diffraction in the particulate medium; the particles are opaque.

The overall reflection model in the CentRec can be divided into two sub-models, namely a short-range and a long-range reflection model. The short-range reflection model accounts for the reflections within the particle film in short particle–particle distances while the long-range reflection model corresponds to the reflection from the particle bulk to other parts of the particle film, large surfaces of the cavity and the aperture plane. The short-range reflections and the thermal emission due to the particle temperature difference have been modelled with a simplified distance-based approach previously for gray and diffuse particles [25,26]. In Fig. 2, the types of the long-range reflection from the particle film are schematically shown. Note that the portion of the reflection going to metallic parts of the receiver and the particle film, i.e. reflections labeled as 2,3 and 4 in Fig. 2, may be either re-reflected to other parts of the receiver or absorbed by these parts of the receiver.

In the CentRec application, sintered bauxite particles are preferred as particulate material due to their good optical and thermal properties. Jeong et al. [27] found that the absorptivity of a single particle layer formed by non-touching particles like in a falling particle curtain changes negligibly in the wavelength range from 380 nm to 1020 nm. It is also found that the ceramic bauxite particles have a specularity of 0.2, meaning that reflections from a particle surface is mostly diffuse, not specular. Thus, the individual particles' surface is assumed to be gray

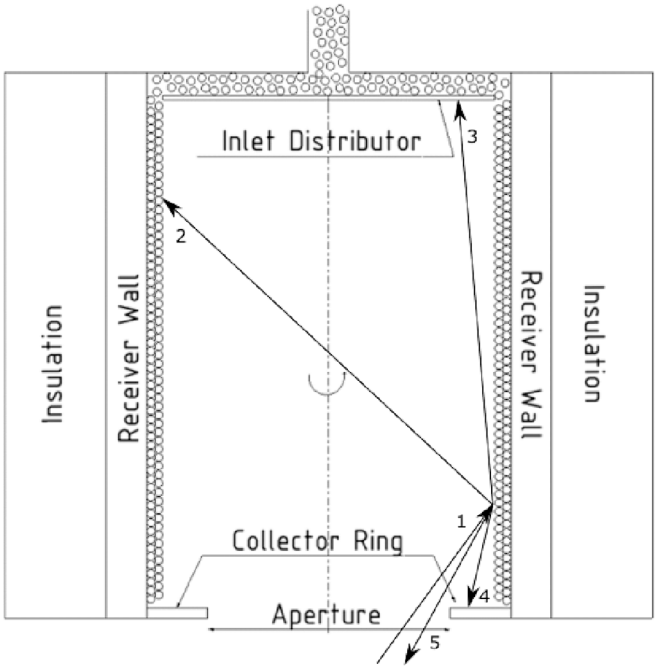

Fig. 2. Schematic cross-sectional view of the CentRec along with the representative rays: (1) solar irradiation, (2) reflection to another part of the particle film, (3) reflection to the inlet distributor, (4) reflection to the collector ring, (5) reflection to the aperture, i.e. reflection loss.

and diffuse due to their rough and dull surface for the sake of simplicity in this study. The particles are also assumed as perfect spheres. Although the particle surface is assumed as diffuse for reflections, the previous study of the authors showed that reflection from the particle film is not diffuse, but highly dependent on the incidence angle of the incoming rays [25]. In that study, it is found that if diffuse reflection from the particle bulk is assumed for the CentRec, the reflection loss through the aperture is underestimated by 50 % compared to MCRT results. This is mainly because the surface of the film is not flat, but consists of many spheres. Thus, the reflection needs to be modelled as incidence angle dependent.

Johnson et al. [24] calculated the bed absorptivity for a wide range of the absorptivity of the diffuse and gray particles, the incidence angle and the solid fraction by applying fully resolved MCRT to randomly generated particle beds with uniform solid fraction, created in LIGGGHTS. In Fig. 3, the bed absorptivity (α_{bed}) is plotted against the particle absorptivity for various incidence angles by using the curve fit developed in [24]. Note that the representative bed solid fraction for the CentRec is found as 0.5. The bed reflectivity can simply be assumed as ($1 - \alpha_{bed}$) because negligibly small energy reaches the cavity wall for an opaque particle film, eventually the transmissivity of the particle bed is zero.

Jeong et al. [27] found the spectrally averaged (380 nm to 1020 nm) absorptivity of individual bauxite particles as around 0.88 while forward and backward scattering are found as ~ 0.04 and ~ 0.08, respectively. Sutter et al. [28] measured the solar-weighted absorptivity (AM1.5) of 5 different bauxite fixed bed samples to be in the range of 0.835–0.944. Similarly, Siegel et al. [29] used packed bed pellets of 4 different sintered bauxite samples, and measured solar-weighted absorptivity (AM1.5) to be 0.895–0.931. Note that the values from [28,29] are not single particle properties, but found for packed pellets. As a reference value, the bed absorptivity of the packed bed pellets in the measurement studies is assumed as 0.92. Because the samples are packed in these studies, being different than the CentRec case where the bulk particles are in motion, the bed solid fraction of packed pellets can be assumed as 0.6. The incidence angle was reported as $8^\circ - 20^\circ$ in the study of Sutter et. al [28]. According to Fig. 3, these rough values correspond to a single particle absorptivity of about 0.86, and this value is also assumed as solar-weighted particle absorptivity throughout this study.

The thermal emission is omitted in this study because the new model focuses on the derivation and validation of the reflection model. The reflection of the emitted thermal radiation from the particles inside the cavity is also not considered. However, in another study of the authors [9], it is shown that the diffuse particle film surface assumption in a radiation enclosure gives very similar results to the results of a MCRT-based thermal emission model in terms of emission loss through the aperture. Therefore, the emissive heat exchange between large surfaces (particle film, collector ring, inlet distributor etc.) can be assumed to occur as diffuse.

2.1. Direction-Dependent hemispherical reflection distribution

In Fig. 4, the local coordinate system for a particle film section along with zenith and azimuth angles of generated (or incident) and reflected rays are represented. The azimuth angle (θ) varies between 0 and 2π while zenith angle (γ) does between 0 and π/2. The zenith angle of the generated rays (γ_{gen}) can also be named as incidence angle. To show

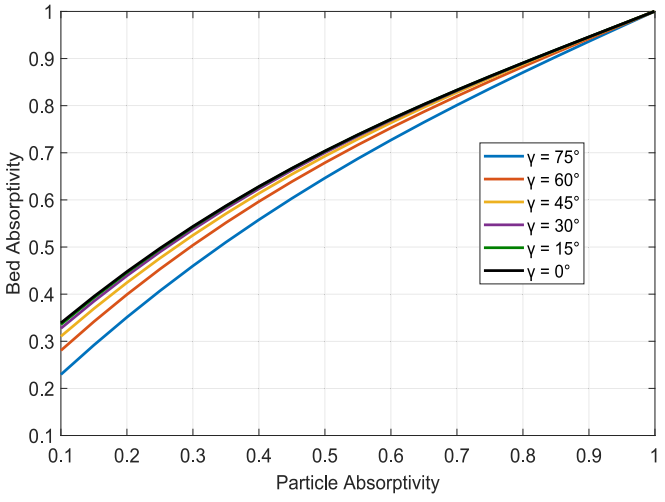

Fig. 3. Bed absorptivity vs. particle absorptivity for various incidence angles [24]. Solid fraction is 0.5.

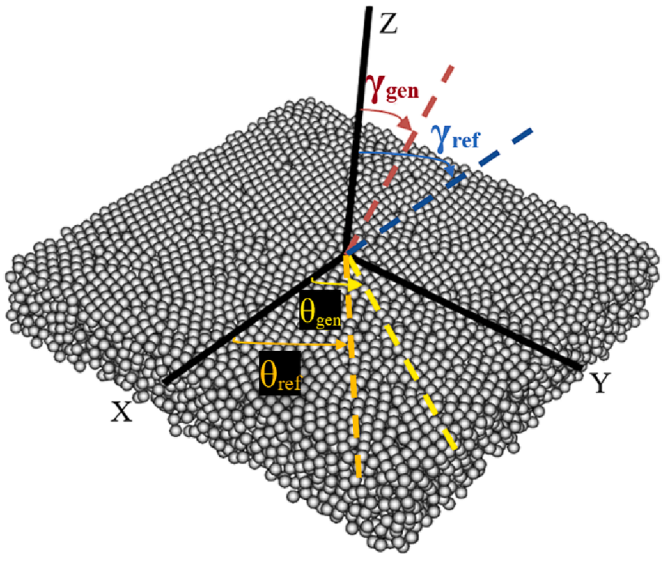

Fig. 4. The local coordinate system to be used in the reflection model.

directional dependence of the reflection from the particle bulk, firstly, a particle domain with a lateral dimension of 40 particle diameters (d_p) is created in LIGGGHTS. The bed thickness is set to 10 d_p. For this purpose, as many particles as needed to provide a bed solid fraction of 0.5 are generated in a DEM domain whose boundaries are specified as periodic, so that particles leaving the domain from a surface boundary reenter the domain from the surface boundary on the opposite side, as explained in more detail in [24]. With a given initial velocity and restitution coefficient of 1, particles are let to move and collide indefinitely in a zero-gravity domain without kinetic energy loss. After a sufficient time, the particle bed porosity is uniform in all directions. To check this, the solid fraction of many randomly selected sub domains from the simulation box are compared to each other to make sure that the solid fraction does not vary across the simulation box. Then, a snapshot of the particle positions is taken. As a next step, parallel rays are generated with a certain incidence angle γ_{gen} and azimuth angle θ_{gen} and directed towards the particle domain. For this purpose, a validated MCRT code being available in GitHub [26,30,31] is utilized and slightly modified to track the reflected rays with their angle γ_{ref} to the normal of the particle domain and with their azimuth angle θ_{ref}.

Fig. 5 shows the trajectories of 50 parallel incident rays with an incidence angle of 65° (red) and their reflection vector (yellow) from the generated particle bed comprised of diffusely reflecting particles. In Fig. 5, it can be noticed that the reflection behavior of a particle bed surface differs significantly from the one of a diffuse flat surface where the reflection goes to all directions uniformly. The fact that the reflection tends to be in the direction where the incident rays come from mainly is a result of the spherical nature of the particles, resulting in a very rough particle film surface. Note that even realistic non-spherical particles may result in such behavior, but the reflection distribution would be particle shape-dependent and slightly different than the one for spherical particles.

Similarly, in Fig. 6, the generated (red) and reflected (black) rays are shown for 3 different incidence angles, but this time a 2D projection of the reflected rays is plotted, although the reflected rays travel in the 3D domain. The generated parallel rays have an azimuth angle of 180°, so they lie in the xz-plane. From Fig. 6, it can be noticed that as the incidence angle of the generated rays increases, the rays are less likely reflected to the opposite side of the film. It should be noted that rays can also be reflected back after several reflections within the particle film.

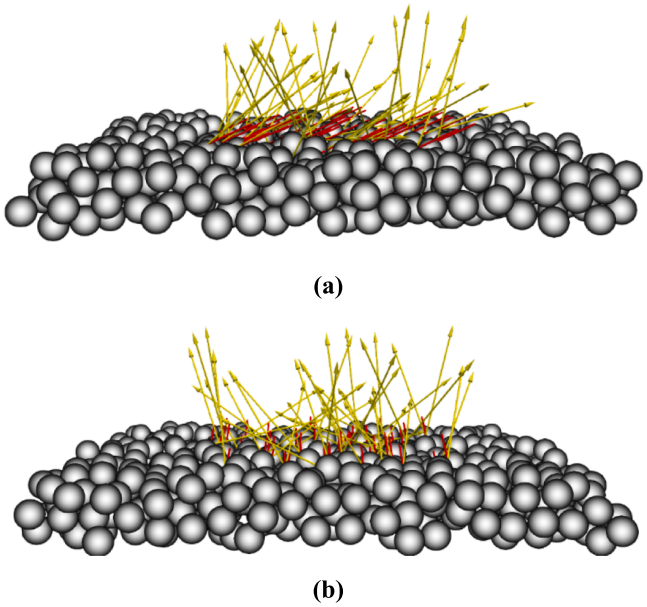

Fig. 5. Representation of randomly selected 50 incoming rays (red) with an incidence angle of 65° and their reflections (yellow) from a 10 d_p x 10 d_p particle film section. **(a)** Side view **(b)** Front view.

In Fig. 7, a more detailed look on the direction-dependent hemispherical distribution of the reflected rays, or more widely known the Bidirectional Reflectance Distribution Function (BRDF), is presented for several incidence angles of the generated rays. The BRDF is, by definition, a function of five different variables, namely the wavelength, azimuth and zenith angles of incident and reflected rays [32]. Because the particles are assumed as gray, and the generated particle bed is isotropic in the lateral directions, the BRDF is only three dimensional in this study: it is a function of the zenith angle of the incident rays and of the zenith and azimuth angles of the reflected rays. It is approximated numerically by tracing 150 million parallel rays from a fixed azimuth angle of 180° and a given zenith angle. The energy of the rays $\Delta\dot{Q}_{ref}$ reflected to a certain direction (γ_{ref}, θ_{ref}) within an angle increment of $\Delta\gamma_{ref} = \Delta\theta_{ref} = 1°$ is counted. Then, the BRDF is calculated as follows.

$$BRDF = \frac{1}{\cos\gamma_{ref}\sin\gamma_{ref}\Delta\gamma_{ref}\Delta\theta_{ref}} \cdot \frac{\Delta\dot{Q}_{ref}(\gamma_{ref}, \theta_{ref})}{\dot{Q}_{gen}(\gamma_{gen})} \quad (1)$$

Fig. 7 shows a quite diffuse reflection for an orthogonal irradiation of the particle bed ($\gamma_{gen} = 0°$). For a perfectly diffuse reflection, the BRDF would be constant and would equal to the hemispherical reflectivity divided by π [33], which would be 0.033 in our case. Reflection to low and very high zenith angles is only slightly favored over other reflection directions. One can also see no favored azimuth angle, which is expected due to symmetry. As the incident ray direction becomes less perpendicular to the particle bed surface with increasing γ_{gen}, the BRDF becomes less uniform and the reflection more specular. The rays are reflected more and more towards the direction of the incoming rays in azimuth direction and have the prevalence to be reflected to high zenith angles in general. This prevalence is more pronounced for higher γ_{gen}.

To use it later in the simplified model, the BRDF of the reflected rays was calculated for a range of $0° \leq \gamma_{gen} \leq 85°$ with 5° intervals, in total for 18 cases. Note that there is no solution for $\gamma_{gen} = 90°$ because the generated rays are parallel to the surface of the particle film for that case. Moreover, there is no need to consider different θ_{gen} because the particle film is isotropic in terms of packing structure in lateral directions. θ_{ref} is directly dependent on θ_{gen}, so a derivation for a reference value of θ_{gen} is enough.

For each case, 150,000,000 rays are generated and sent to the generated particle domain. Depending on the incidence angle, 8 – 10 % of the rays are reflected for a particle absorptivity of 0.86. The BRDF values corresponding to each zenith and azimuth angles of the reflected rays are recorded in a matrix with size of 90 x 360 elements for each γ_{gen}. After obtaining the reflection matrix for each case, the resultant reflection matrix "R" has a dimension of 90 x 360 x 18 such that the first dimension is γ_{ref}, the second one is θ_{ref}, and the third one is γ_{gen}. Note that the matrix "R" is derived for a particle absorptivity of 0.86 and bed solid fraction of 0.5, being representative for the CentRec application, in this study. However, one can calculate the matrix "R" also for other particle absorptivities and bed solid fractions. The general flow diagram of the reflection calculations for the CentRec is represented in Fig. 8.

2.2. Application of the derived reflection distribution to the CentRec

The main reason of deriving the reflection matrix is to avoid running the costly MCRT algorithm in the particle domain. To do so, it is assumed that the solar irradiation is reflected from the discrete curved surfaces comprising the particle film surface, not from individual particles. There is a significant difference in the computational effort between running MCRT in a domain comprised of millions of particle surfaces and a hollow-cylinder-like curved surface. For the purpose of representing the absorbed power distribution, the particle film is discretized in axial and tangential directions into many volumes, as seen in Fig. 9. The inward surface of the discrete volumes is referred to as "mesh elements".

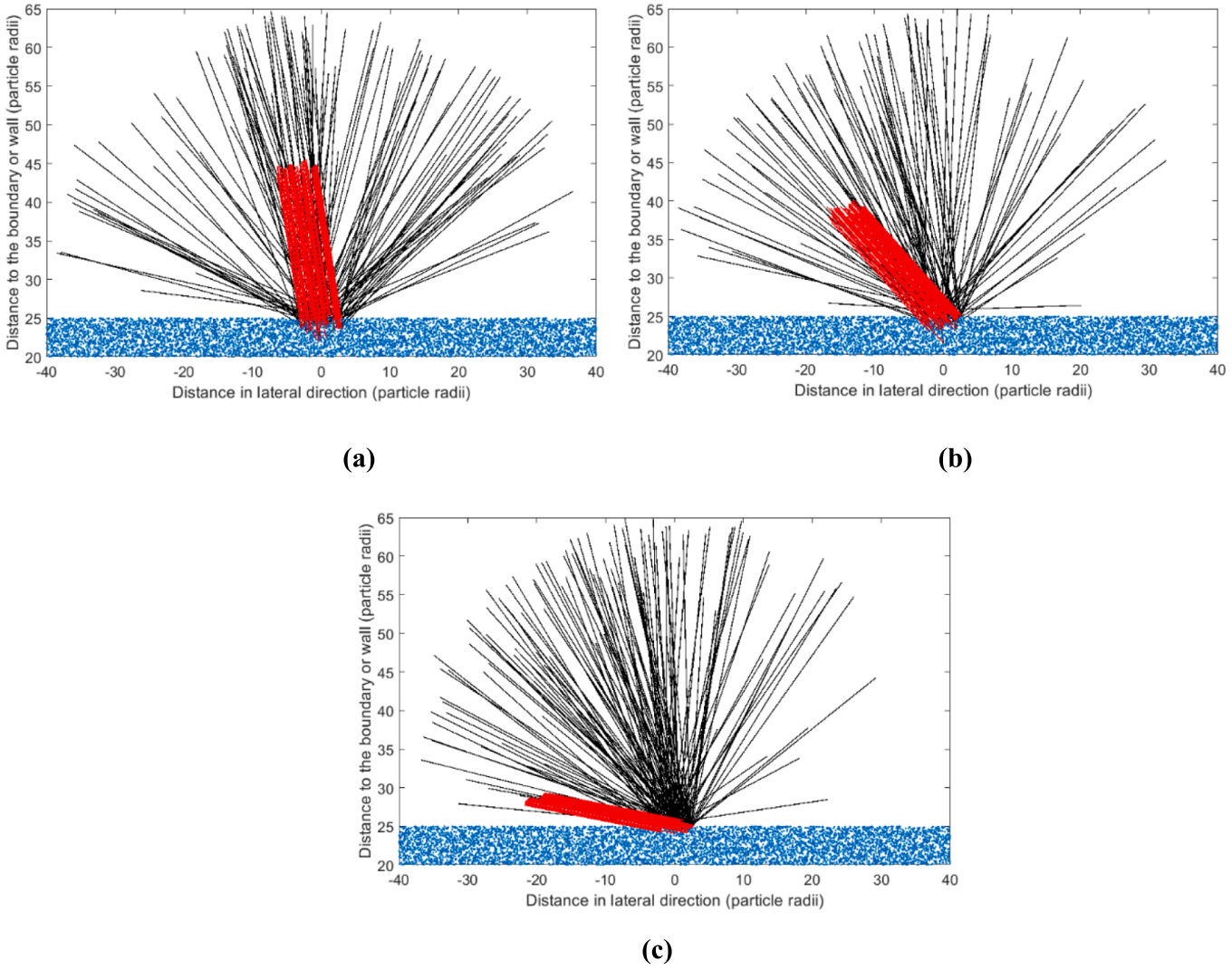

Fig. 6. Representation of generated parallel rays (red) and reflections from the particle film (black) for (a) $\gamma = 10°$ (b) $\gamma = 45°$ and (c) $\gamma = 80°$. The blue dots represent particles' center.

For the simplified raytracing approach the DLR-owned software tool SPRAY (Solar Power Raytracing Tool) was modified to enable the use of the previously determined reflection matrix. SPRAY is based on the Monte Carlo ray tracing approach and is designed for high flexibility for a huge variety of applications in concentrating solar thermal systems. In the given application, the features for the detailed simulation of a solar tower system are used as a basis. SPRAY was then extended to enable the computationally effective use of the directional reflection information. The extension includes mainly the following aspects:

- Data input: reading the reflection matrix "R" from a text file
- Receiver representation: a specific 3D receiver model was created describing a CentRec-type receiver with a cylindrical cavity, a backwall (inlet distributor) and a front shield (collector ring), with variable dimensions
- Implementation of the incidence angle dependent particle film reflectivity
- Implementation of the calculation of the reflected ray directional distribution, based on Monte Carlo ray tracing principles. The applied procedure is as follows:
  - o Symmetry is applied for the azimuth angle of the reflected ray to reduce stochastic effects in the results of MCRT.
  - o Generation of a 1-d reflection probability array for each ray incidence angle: Incremental summing up the probability values for each combination of the reflected zenith and azimuth angles, with logging of the related angles with each increment; each array element then represents a specific angle range for zenith and azimuth angle of the reflected ray

The most important steps during a SPRAY simulation run are as follows.

- Data input: configuration of the heliostat field, receiver, tower; directional reflection characteristics of the particle film; site and time point information.
- Raytracing:
  - o A huge number of rays (216 Million rays) is generated on the heliostat surfaces, and then traced towards the receiver, taking shading, blocking, atmospheric attenuation and intercept losses into account; rays are generated on discretized heliostat facets with a power defined by the area of the facet element, the mirror reflectivity, the actual direct normal insolation and the cosine of the incidence angle onto the facet surface.
  - o If a ray hits a mesh element of the discretized receiver:
    - ■ Determine incidence angle of ray on mesh element

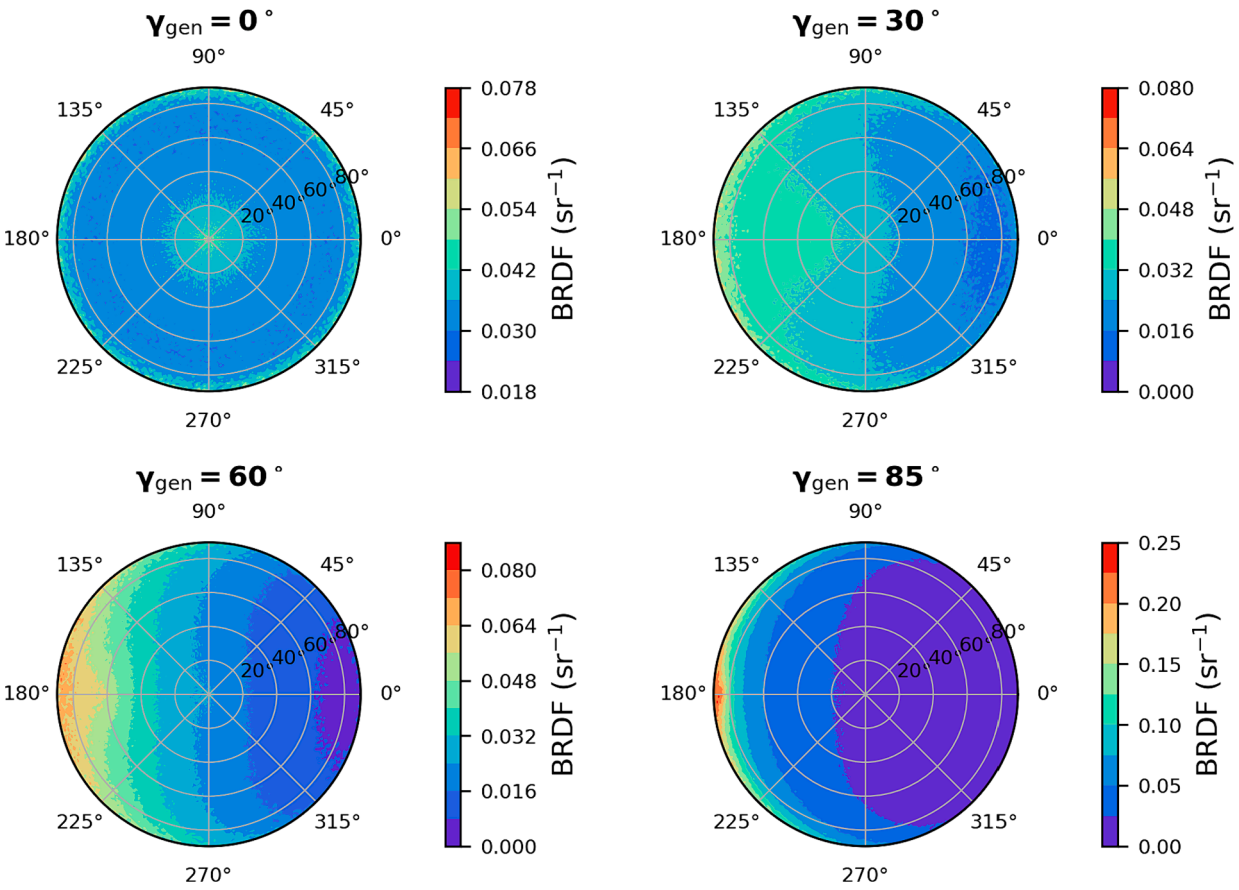

Fig. 7. Bidirectional reflectance-distribution function (BRDF) for four different zenith angles of incoming radiation γ_{gen}, particle bed void fraction of 0.5 and particle absorptivity 0.86. The incoming radiation has an azimuth angle θ_{gen} of 180°.

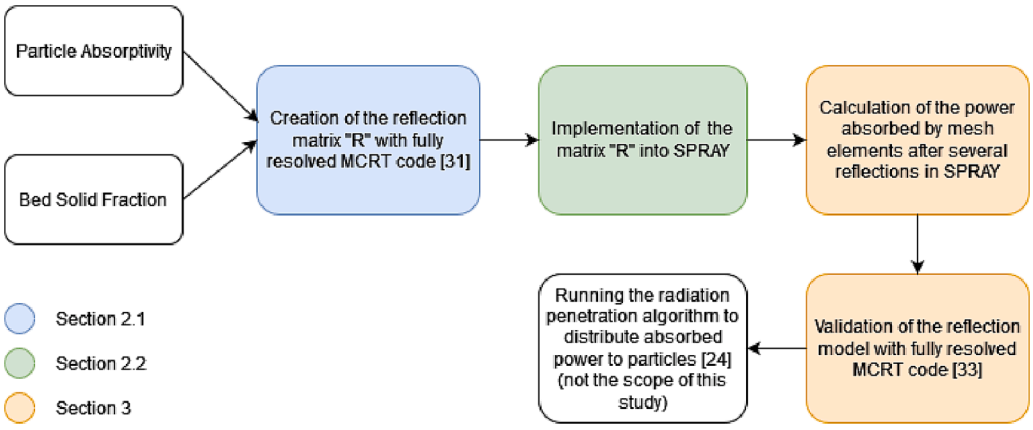

Fig. 8. Flow diagram of reflection calculations for the CentRec.

- Determine film reflectivity as function of incidence angle
- Determine if ray is reflected, using Monte Carlo principles.

o If a ray is reflected:

- Determine azimuth of the incoming ray on the mesh element surface
- Find the upper-closest incidence angle considered in the derivation, e.g. for 28°, use 30° and for 31° use 35°
- Use reflection characteristics for this incidence angle in reflection matrix "R"
- Calculate the azimuth and zenith angles of the reflected ray using Monte Carlo principles

o Raytracing is then continued with the reflected ray until the ray is absorbed or exits through the receiver aperture.

o If ray is absorbed or exits, the corresponding ray power is summed up for each mesh element.

Monte Carlo principles are based on generating random numbers for reflection probabilities given each zenith and azimuth ranges in reflection matrix "R". For a sufficiently large ray count, the stochastic error can be reduced to a negligible amount.

The main result of a SPRAY simulation is the discretized distribution of the power absorbed by the mesh elements, the backwall and the inner side of the front shield. The power loss through the aperture is also

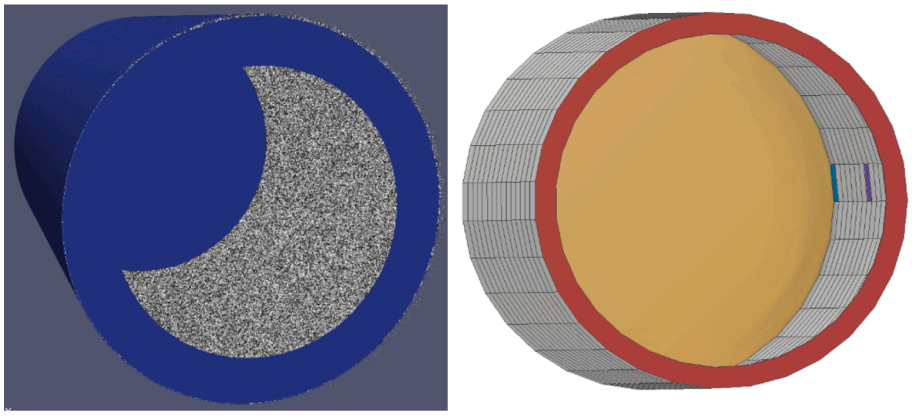

(a) (b)

Fig. 9. **(a)** Particle film flow in a CentRec simulation for a cavity diameter of $100d_p$. **(b)** Meshed particle film surface. The back – yellow surface is the inlet distributor and the front – red surface is the collector ring.

recorded. This data is then used by the radiation penetration algorithm [24] to determine the distribution of the absorbed power to the individual particles.

The mesh elements need to be created on the particle film surface, not on the cavity wall because the thickness of the particle film slightly reduces the effective cavity diameter. For this reason, the particle film thickness has to be calculated before the SPRAY calculations. A particle configuration after the system reaches the cold steady-state in the DEM simulation, meaning that the inlet and outlet particle mass flow rate equals each other, is considered. By using the particle positions from a DEM simulation, the average film thickness (t_{film}) can be roughly calculated as follows by assuming being much smaller than the cavity radius.

$$t_{film} = \frac{n_p V_p}{\pi D_{cav} L_{cav} f_s} \tag{2}$$

In Eq. (2), the particle number and volume are denoted as n_p and V_p, respectively. Moreover, the cavity diameter, cavity length and bed solid fraction are denoted as D_{cav}, L_{cav} and f_s, respectively. The effective cavity diameter is then defined as follows.

$$D_{cav,eff} = D_{cav} - 2t_{film} \tag{3}$$

For a given particle absorptivity, wall (inlet distributor and collector ring) absorptivity, film thickness, cavity dimensions and ray distribution, the absorbed energy distribution on the particle film can be calculated. The mesh element size defines the resolution of the distribution but is also important for a complementary radiation penetration model [24] derived previously by the authors. While the reflection model finds the final energy absorption after reflections by each mesh element, the radiation penetration model distributes this energy to individual particles under the surface mesh elements. Thus, the combination of these two models replaces MCRT to model the solar irradiation of the particle film.

In the SPRAY MCRT model atmospheric losses are accounted for the ray path up to the receiver aperture, but neglected inside the receiver cavity. This is justified as the travelled ray distances are much smaller than from the heliostats to the receiver. In addition, the air temperature inside the receiver is high and thus the air density is low, leading to reduced atmospheric absorptivity.

2.3. Resolved Monte Carlo ray tracing on particle scale

To validate the reflection model, a resolved MCRT simulation was performed on the particle scale with an in-house C++ code [34]. The code can be coupled to LIGGGHTS to include heat transfer mechanisms like particle–wall conduction, inner-wall conduction and in particular radiation, both thermal emission and incoming solar radiation. Here, we only use the latter feature of the code to determine the reflection loss. In the code, surfaces are assumed to be gray and diffuse. Walls are described by triangulated surface meshes in STL-format, particles by spheres, loaded from a LIGGGHTS dump file. The code is parallelized, runs on Linux and has been validated by several analytical test cases. For more information, it is referred to [34].

Here, the code is used to trace rays coming from the heliostat field (generated by SPRAY), with the purpose to determine if and where they are going to be absorbed in the receiver or if they leave the receiver through the aperture (reflection loss). Therefore, meshes in STL file format were generated for the back wall, for the cylindrical cavity wall and for the collector ring.

3. Model optimization and validation

As a representative test case for validating the reflection model, a configuration with a centrifugal particle receiver installed at the DLR solar tower test facility in Jülich was selected. A realistic flux distribution on the aperture plane is calculated in SPRAY by considering 1996 heliostats, each having a surface area of 8.2 m^2. Related receiver parameters are listed in Table 1. Note that a film thickness of 4.58 d_p gives an effective cavity diameter of 0.789 m. The walls of the receiver are treated as diffusely reflecting surfaces.

The developed model is compared with the resolved MCRT model described in section 2.3 for one specific particle arrangement, taken as a snapshot from one time instant of the DEM simulation of the steady particle flow through the CentRec. As the new model and the resolved MCRT model are both fed with the same information (i.e. particle positions) and the particle flow is in steady state, it is not expected that the

Table 1
Parameters considered in model application.

Parameter	Unit	Value
Cavity Length	m	1.2
Cavity Diameter	m	0.8
Aperture Diameter	m	0.6
Particle Diameter	mm	1.2
Particle Absorptivity	–	0.86
Wall Absorptivity	–	0.4
Particle Film Solid Fraction	–	0.5
Particle Mass Flow Rate	kg/s	0.5
Receiver Rotation Speed	rpm	62
Particle Film Thickness	d_p	4.58

deviation between the models is substantially different at another time instant.

3.1. Dependency of resolved MCRT results on ray count

The receiver parameters listed in Table 1 result in about 8.8 million particles at cold steady state. The resolved ray-tracing for validation was performed with 10 k, 100 k, 1 million and 10 million rays and each time repeated ten times, so 40 simulations were performed. Fig. 10(a) shows the setup with the three STL meshes and the particles. In Fig. 10(b) one can see that the radiation is absorbed only in the vicinity of the particle bed surface and nearly no radiation reaches the deeper particle layers.

Fig. 11 shows the absorbed power distribution for 10 million rays. To make the MCRT results ray count-independent, the standard deviation needs to be reduced to an acceptable amount. In Fig. 12, the standard deviation distribution is plotted for four ray counts and a mesh element size of $L_{cav}/18$, where L_{cav} is the cavity length. Mind the different color bar scales. The standard deviation in Watts is not uniform for the mesh elements, but increases with the absorbed power. On the other hand, the standard deviation in percentage is higher for the mesh elements with less absorbed power because less rays have been absorbed by these elements; thus, the stochastic error is higher. Note that the standard deviation in percentage is defined as the ratio of the standard deviation to the absorbed power for each mesh element. In Fig. 12, it can be noticed that the standard deviation decreases significantly by increasing the ray count. For 1 million rays, the standard deviation in the hot spot is less than 2 % while for 10 million rays is less than 1 %.

To investigate how the standard deviation changes with the mesh element size, two mesh element sizes are considered. Smaller mesh elements having an edge length of $L_{cav}/36$ are obtained by dividing a large mesh element having an edge length of $L_{cav}/18$ into four identical pieces, as depicted in Fig. 13(a). In Fig. 13, the decrease in the standard deviation (in percentage) with increasing ray count is plotted in log–log scale for the mesh elements which absorbed the most and the least power

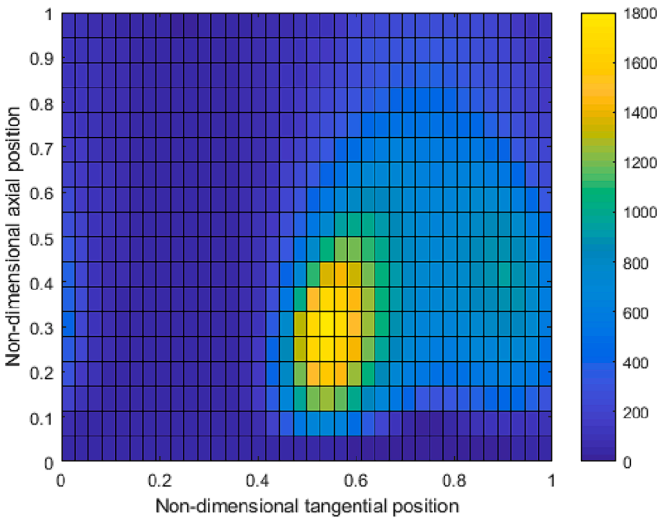

Fig. 11. The absorbed power distribution for mesh element size of $L_{cav}/18$ and ray count of 10 million. The color bar is in Watts. The non-dimensional axial positions of "0″ and "1" correspond to the particle outlet (on the collector ring) and particle inlet of the receiver (on the back wall), respectively (See Fig. 10(a)).

from Fig. 11. In the same figures, results for a smaller mesh elements are also plotted. The results show a linear relation between log scales of the standard deviation and the ray count. Moreover, the standard deviation decreasing with increasing mesh element size can also be noticed in Fig. 13. One can select the appropriate ray count depending on the amount of precision needed. In this study, 10 million rays are selected because the MCRT results will be used as the validation case of the new reflection model.

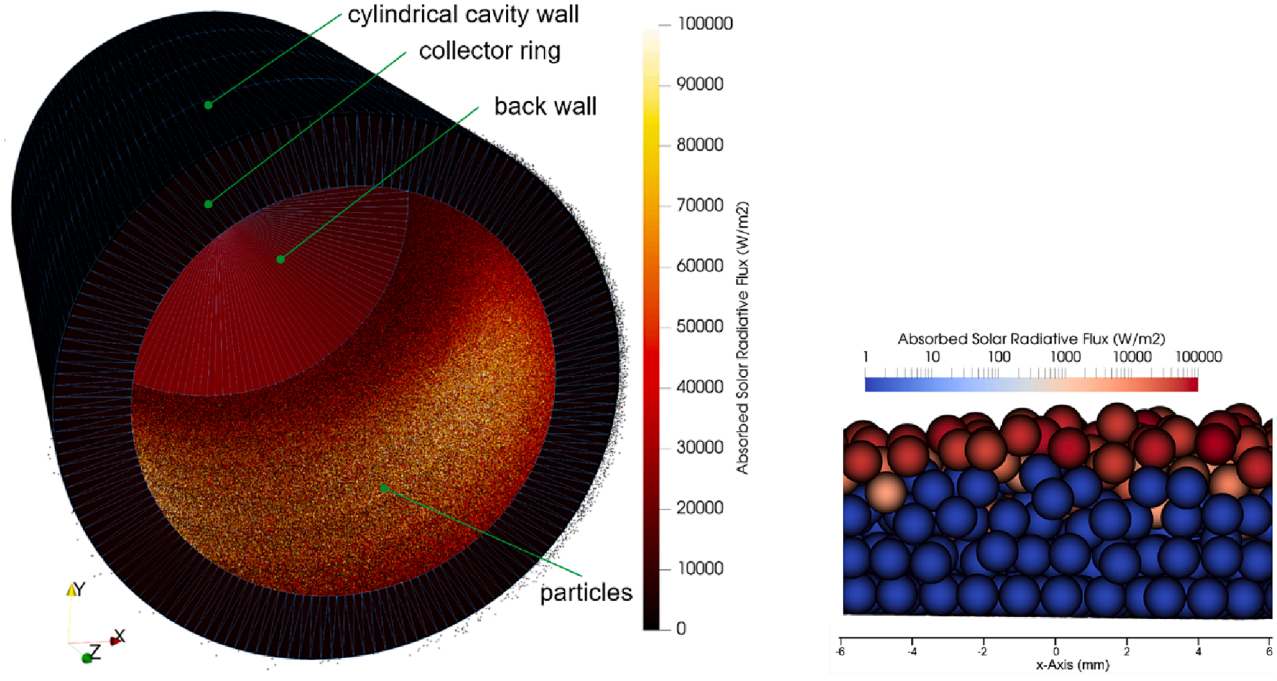

Fig. 10. Resolved MCRT simulation with 10 million rays. **(a)** absorbed flux density in entire receiver **(b)** Detail at z = 0.9 m at the bottom of the receiver (y negative).

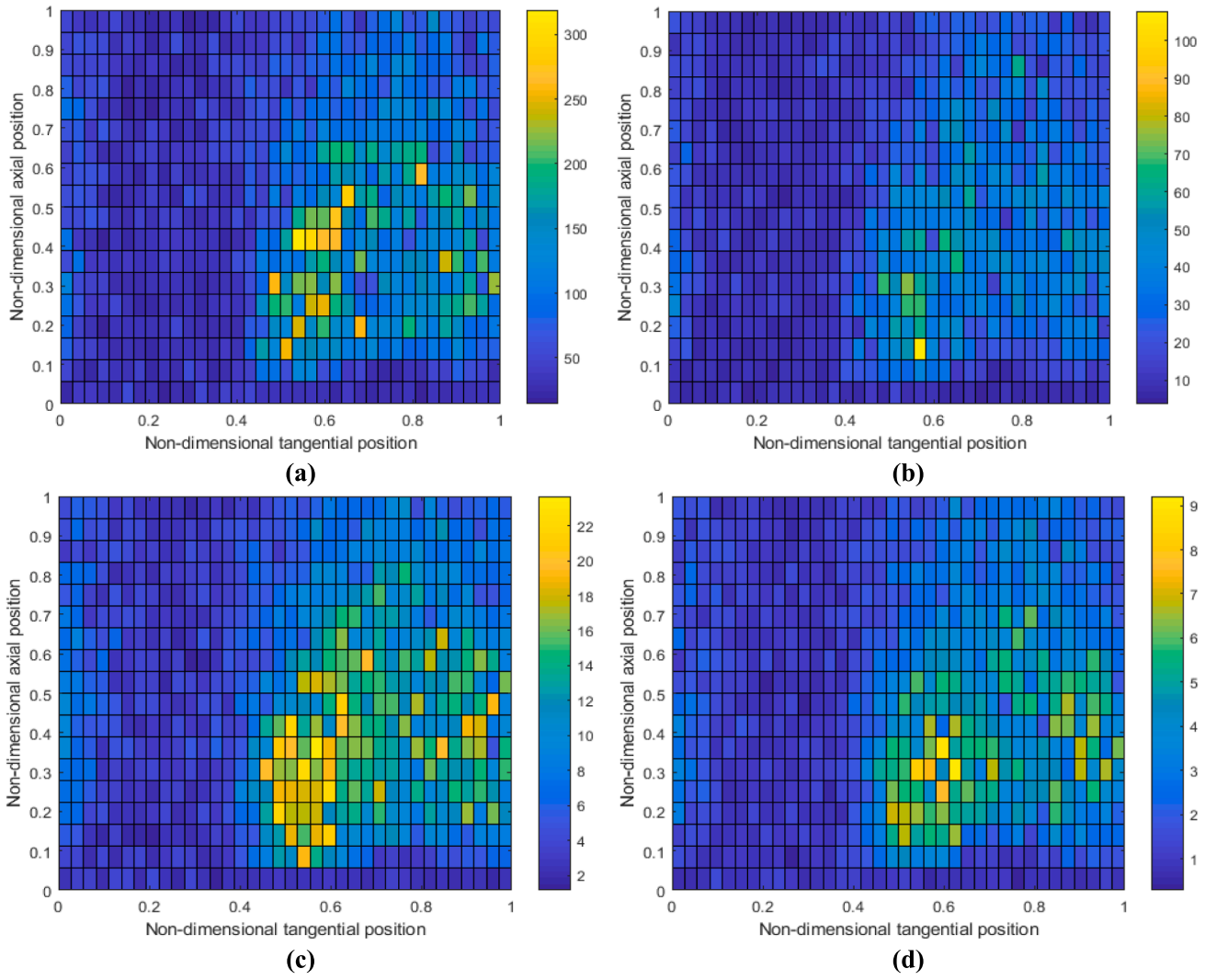

Fig. 12. Mean standard deviation distribution of absorbed power of 10 cases for a mesh element size of $L_{cav}/18$. The ray count is **(a)**10,000, **(b)**100,000, **(c)** 1,000,000 and **(d)**10,000,000. The color bar is in Watts. The non-dimensional axial positions of "0″ and "1" correspond to the particle outlet (on the collector ring) and particle inlet of the receiver (on the back wall), respectively (See Fig. 10(a)).

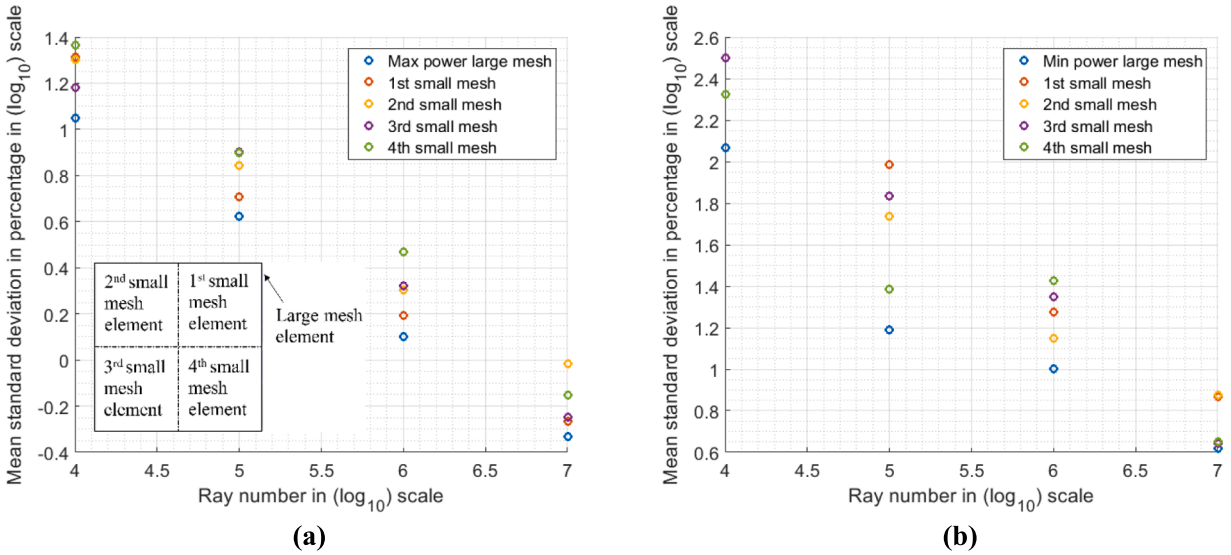

Fig. 13. Mean standard deviation in percentage for the mesh elements absorbing **(a)** the maximum **(b)** the minimum power. Both scales are logarithmic.

3.2. Mesh element size

The mesh element size is an important modeling parameter for the radiation penetration algorithm [24] because the absorbed power is assumed to be uniform on the surface of the mesh element. Thus, the element size should not be very large for the transition regions of the CentRec, e.g. transition from the directly irradiated hot spot to the indirectly irradiated regions. In this study, a uniform mesh element size is selected for the sake of simplicity but a varying mesh element size can also be considered in further optimization studies. The complementary radiation penetration model has been validated for a mesh element size of $50d_p$ x $50d_p$; thus, similar mesh element sizes are compared in this study.

The reflection model explained in Sections 2.1 and 2.2 is applied to the CentRec for the parameters listed in Table 1. In Fig. 14(a) and (b), the absorbed power distribution is shown for mesh element sizes of $L_{cav}/18$ and $L_{cav}/36$, which corresponds to ~ $56d_p$ and $28d_p$. In Fig. 14(c) and (d), the total reflections from the particle film are plotted for two different mesh element sizes. The reflection from the particle surface is simply found by subtracting the power absorbed by a mesh element from the solar irradiation to a mesh element. Positive value means that reflection is from a mesh element while minus means that sum of the reflections from all other mesh elements is to a mesh element and eventually absorbed by that mesh element.

To compare the results of the different mesh element sizes in a quantitative manner, sub-mesh elements are created for each larger mesh element such that the sub-mesh element size corresponds to the smaller mesh element size. The power absorbed by the larger mesh element is split to the uniform sub-mesh elements equally. Fig. 15 reveals the difference between the absorbed power of the smaller mesh elements and a sub-part of the larger mesh elements. The results show that using a smaller mesh element size slightly increases accuracy on the transition region from the directly irradiated to the non-irradiated part of the film. Especially near the outlet, some portion of the large mesh element is irradiated while some is shaded by the collector ring. This results in a non-uniform absorbed energy distribution on the mesh elements located in this transition region, and this effect can be better captured by reducing the mesh element size. However, the maximum difference shown in Fig. 15 is negligibly small compared to the absorbed power shown in Fig. 14(b). Thus, a mesh element size of $L_{cav}/18$ gives sufficiently accurate results for the reflection model.

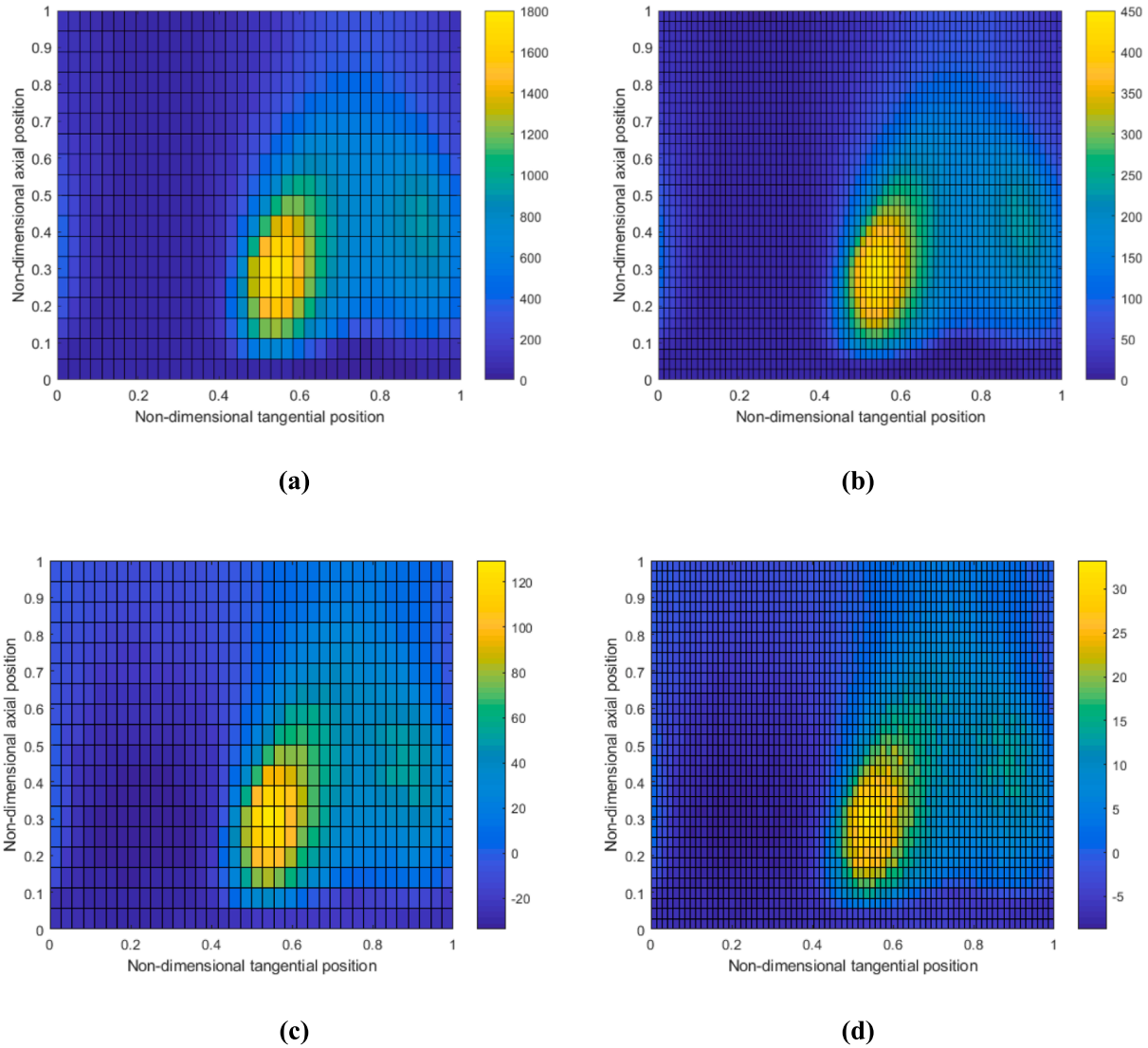

Fig. 14. The amount of **(a)(b)** absorbed and **(c)(d)** reflected power distribution for mesh element size of **(a)(c)** $L_{cav}/18$ and **(b)(d)** $L_{cav}/36$. The color bar unit is Watts.

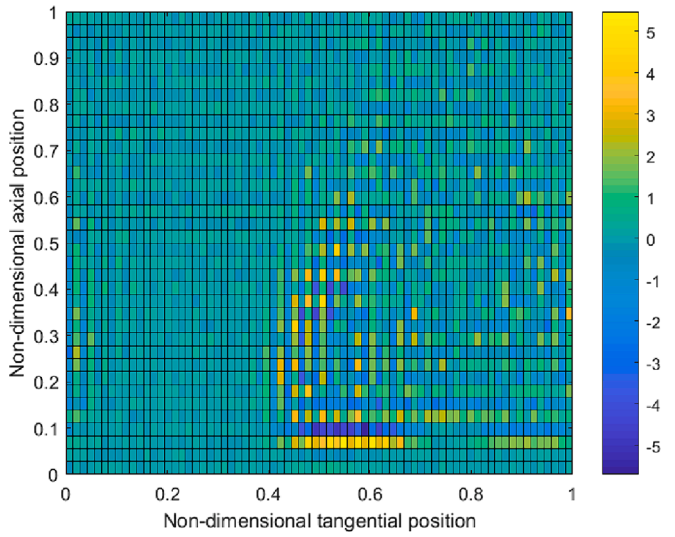

Fig. 15. Absorbed energy difference between the cases for mesh element sizes of $L_{cav}/18$ and $L_{cav}/36$. The color bar unit is Watts.

3.3. Model comparison

To validate the new model, its results are compared to MCRT simulations resolving the entire particle film, see section 3.1. In Table 2, for the given flux distribution and the CentRec case tabulated in Table 1, the energy absorbed by the particle film and the receiver components are compared. The results show that the new model can predict the reflection loss and the energy absorbed by the particle film and other components with very high accuracy. The transmissivity of the particle film is assumed as zero because the particle film is thick enough ($>4d_p$). For this reason, the power absorbed by the wall is simply set to zero. However, after running the radiation penetration algorithm, the power going to the wall can also be calculated and compared with the resolved MCRT result. In Fig. 16(a), a more detailed comparison is made in terms of power absorbed by mesh elements. The new model overestimates the absorbed power next to the particle inlet (topmost row) while underestimating it at the section where the particles are first introduced to the receiver (region enclosed by red dashed lines). This inconsistency is mainly due to the fact that the particle film is not fully formed next to the particle inlet, i.e. particle film thickness and porosity changes significantly in tangential direction before the first rotation of the particles is completed. Note that the new model assumes a uniform film thickness in the receiver; thus, the more variation in the film thickness, the more the reflection model deviates from the MCRT results. However, this "inlet effect" does not affect the overall results considerably because the inlet region of the receiver is not irradiated by the concentrated solar energy directly. In Fig. 16(b), the difference between two approaches is also presented in percentage. The reflection model accuracy is best checked in the not-directly-irradiated region because these mesh elements absorb only the reflected power from the other parts of the particle film and large surfaces of CentRec. If the mesh elements next to the particle inlet are excluded, the average difference is around 2 %. The main reason of this slight error is the assumption that the film thickness is uniform in tangential and axial directions. However, there is a variation in the film thickness in the axial direction [35].

Table 2
Comparison of the resolved MCRT simulation and the new model regarding the energy absorbed by the receiver components.

	MCRT (10 million rays)		New Model	
	kW	%	kW	%
Intercepted power	237.72		237.78	
Power absorbed by particles	223.05	93.83	223.63	94.05
Power absorbed by collector ring	0.82	0.34	0.79	0.33
Power absorbed by backwall (inlet distributor)	9.82	4.13	9.68	4.07
Reflection loss through aperture	3.81	1.60	3.67	1.54
Power absorbed by cylindirical cavity wall	0.22	0.09	–	–

The computational time required for the reflection model and resolved MCRT should also be compared because the main reason for deriving the reflection model is to avoid costly MCRT simulations in the particle domain. However, the reflection model is only comparable with the resolved MCRT simulations if the computational burden resulting from the radiation penetration algorithm is also considered. This is because in the resolved MCRT simulation, the solar irradiation is already distributed to individual particles while the reflection model only finds the power absorbed by the mesh elements. Thus, the reflection model is coupled to the radiation penetration algorithm in order to distribute the power absorbed by the mesh elements to the individual particles. In Fig. 17, the run time of resolved MCRT simulation for the considered ray counts is shown. Resolved MCRT simulations were run on 28 cores of an Ubuntu workstation (2x Intel Xeon E5-2697v3, 64 GB DDR4 RAM). The run time is a linear function of the ray count. The results show that tracing 10 million rays in the particle domain requires around 11 h.

The run time of the SPRAY simulations used to find the absorbed power on the mesh elements for the given reflection characteristics also scales linearly with the ray count. 215 million rays were generated on the heliostat surfaces and around 3.9 million of them cross the aperture plane. The total run time is 145 s on a machine with Core i7-1270(P), 2.20 GHz CPU and 16 GB RAM. Note that SPRAY calculations do not depend on the mesh element size. However, the run time of the radiation penetration algorithm changes with the mesh element size as shown in Table 3. For a mesh element size of $L_{cav}/18$, the run time of the combination of SPRAY and penetration algorithm is $\sim$ 9 min. Even if 1 million rays are considered in resolved MCRT simulations, there is significant improvement in the computational time required. Moreover, as long as the film thickness and the flux distribution do not change with time, there is no need to recalculate the absorbed power distribution in SPRAY every DEM thermal coupling time step being how frequently the particle temperature change is updated in the DEM heat transfer code due to the reflection model. Thus, the run time of the solar irradiation computation can be reduced to $\sim$ 6 min. Note that the radiation penetration algorithm runs on MATLAB and on a computer with Intel(R) Xeon(R) Platinum 8260 CPU, 2.40 GHz 2 Processors, 192 GB RAM. Considering that the current radiation penetration algorithm is not parallelized well in MATLAB, there is further room for improvement in terms of run time.

4. Conclusion and outlook

In this study, a reflection model has been developed for the CentRec solar particle receiver to avoid computationally expensive resolved MCRT simulations. It has been found that the reflection from a particle bed is neither diffuse nor specular, but incidence angle-dependent because of the spherical surface of the individual particles forming the particle film. For this reason, a Bidirectional Reflectance Distribution Function (BRDF) for a particle bed being representative for the CentRec application has been determined for various incidence angles. Then, the generated reflection characteristics have been imported to the ray tracer SPRAY to find the absorbed power distribution on the particle film. For a ray distribution calculated by taking the heliostat configuration into account, the power absorbed by the particle film and large surfaces of the CentRec such as the collector ring, and the reflection loss has been compared by resolved MCRT simulations, and a very high accuracy has been obtained. Moreover, the absorbed power distribution for the reflection model and resolved MCRT simulations have been compared. Except for the inlet region where the particle film is not fully formed yet, the reflection model has given similar results to resolved MCRT

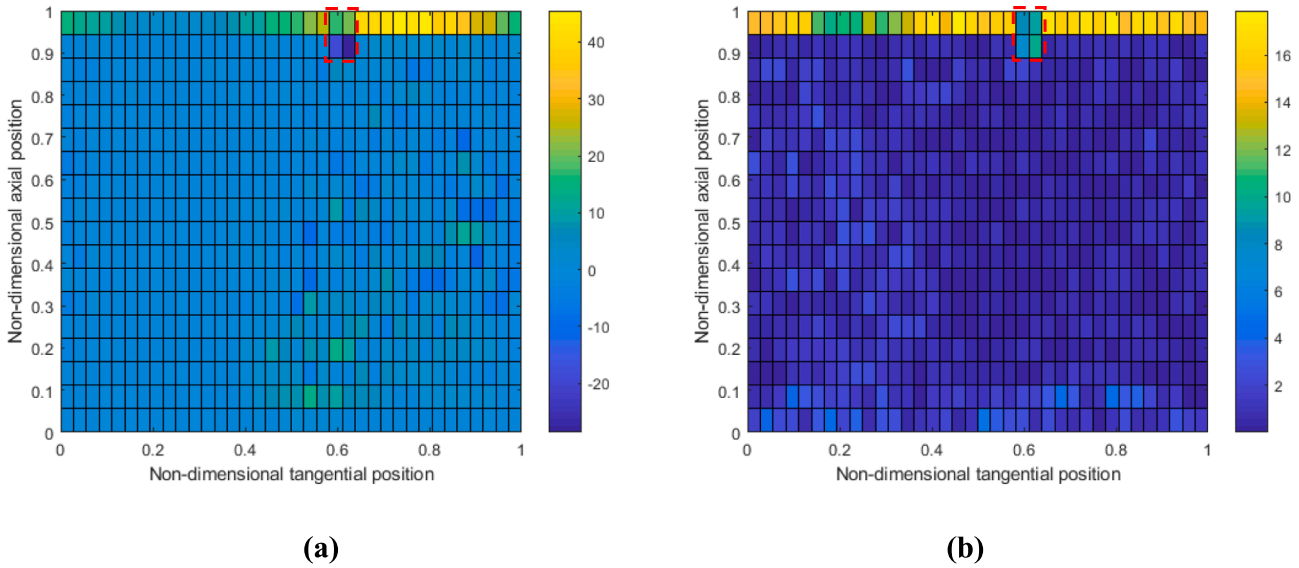

Fig. 16. Absorbed power difference between the reflection model and the resolved MCRT simulation using 10 million rays for mesh element sizes of $L_{cav}/18$. **(a)** The power difference, the color bar unit is Watts **(b)** the absolute percentage difference, the color bar is in percentage. The region enclosed by red dashed lines corresponds the place where fresh particles first touch the particle film.

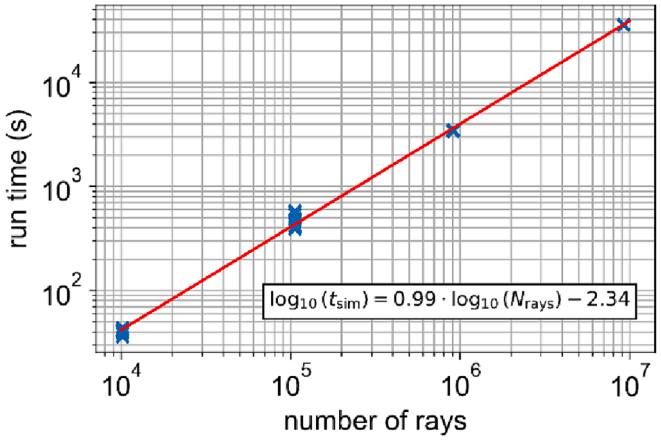

Fig. 17. Run time of the resolved MCRT simulations.

Table 3
Run time for the reflection and penetration algorithm for the case in Table 1.

Mesh Element Size	Number of Mesh Elements	Run time for Radiation Penetration Algorithm (s)	Run Time (Radiation Penetration + SPRAY) (s)
$L_{cav}/9$	162	324	469
$L_{cav}/18$	648	372	517
$L_{cav}/36$	2592	567	712
$L_{cav}/54$	5832	773	918

simulations. The combination of the reflection model calculated by SPRAY and a previously developed radiation penetration algorithm has resulted in significantly lower run time compared to the resolved MCRT simulation for the given computer specifications. However, it is not possible to make direct comparison between the computational times because the computer capabilities (Processor type, RAM etc.) are not similar and different computational tools are employed for simulating the solar irradiation.

The results show that for a realistic flux distribution and aperture ratio of 0.75, being the ratio of aperture to cavity diameter, and cavity length to diameter ratio of 1.5, the reflection loss from the cavity is ~ 1.5 % of the incoming solar irradiation. To reduce the reflection loss, calculations with the new model for various cavity ratios and cavity length to diameter ratios are addressed as outlook. The absorptivity, reflectivity and emissivity of the particles may also change with the temperature and the number of operation cycles. The sensitivity of the particle optical properties on thermal performance of the receiver is also addressed as a future study. The new model will be merged to the in-house DEM Thermal Model of the CentRec to further optimize the particle film conditions and operational conditions.

CRediT authorship contribution statement

Serdar Hicdurmaz: Conceptualization, Methodology, Software, Validation, Data curation, Writing – original draft. **Johannes Grobbel:** Software, Validation, Resources, Supervision, Writing – review & editing. **Reiner Buck:** Software, Validation, Writing – review & editing, Supervision, Project administration. **Bernhard Hoffschmidt:** Supervision, Project administration.

Declaration of Competing Interest

The authors declare that they have no known competing financial interests or personal relationships that could have appeared to influence the work reported in this paper.

Acknowledgements

This work is supported by DLR – DAAD Research Fellowship Programme. The authors also acknowledges Evan Fair Johnson for his effort in modifying MCRT code [31] for reflection calculations.

References

[1] C.K. Ho, A review of high-temperature particle receivers for concentrating solar power, Applied Thermal Engineering 109 (2016) 958–969, https://doi.org/10.1016/j.applthermaleng.2016.04.103.
[2] K. Jiang, X. Du, Y. Kong, C. Xu, X. Ju, A comprehensive review on solid particle receivers of concentrated solar power, Renewable and Sustainable Energy Reviews 116 (109463) (2019) pp, https://doi.org/10.1016/j.rser.2019.109463.
[3] A. Calderón, A. Palacios, M.S.C. Barreneche, C. Prieto, A. Rodriguez-Sanchez, A. Inés Fernández, High temperature systems using solid particles as TES and HTF material: A review, Applied Energy 213 (2018) 100–111, https://doi.org/10.1016/j.apenergy.2017.12.107.

[4] B.H. Mills, C.K. Ho, N.R. Schroeder, R. Shaeffer, H.F. Laubscher, K.J. Albrecht, Design evaluation of a next-generation high-temperature particle receiver for concentrating solar thermal applications, Energies 15 (1657) (2022) pp, https://doi.org/10.3390/en15051657.

[5] T. Lee, S. Lim, S. Shin, D.L. Sadowski, S.I. Abdel-Khalik, S.M. Jeter, H. Al-Ansary, Numerical simulation of particulate flow in interconnected porous media for central particle-heating receiver applications, Solar Energy 113 (2015) 14–24, https://doi.org/10.1016/j.solener.2014.12.017.

[6] W. Wu, A centrifugal particle receiver for high-temperature solar applications, RWTH Aachen University, Aachen, Germany, 2014. Ph.D. Thesis.

[7] C. Tregambi, M. Troiano, F. Montagnaro, R. Solimene, P. Salatino, Fluidized beds for concentrated solar thermal technologies—A review, Frontiers in Energy Research 9 (618421) (2021) pp, https://doi.org/10.3389/fenrg.2021.618421.

[8] R. Thonig, A. Gilmanova, and J. Lilliestam. *CSP.guru*, 01.07.2023, doi: https://doi.org/10.5281/zenodo.1318151.

[9] S. Hicdurmaz, "Numerical and Experimental Investigation of Centrifugal Solar Particle Receiver," Ph.D. Thesis, RWTH Aachen University, 2023 (Under Evaluation).

[10] M. Ebert, L. Amsbeck, A. Jensch, J. Hertel, J. Rheinlaender, D. Trebing, R. Uhlig, R. Buck,, "Upscaling, manufactuirng and test of a centrifugal particle receiver," in *ASME 2016 10th International Conference on Energy Sustainability ES2016*, Charlotte, North Carolina, June 26-30 2016, no. V001T04A007: ASME, doi: https://doi.org/10.1115/ES2016-59252.

[11] L. Amsbeck, R. Buck, M. Ebert, B. Gobereit, J. Hertel, A. Jensch, J. Rheinländer, D. Trebing, R. Uhlig, "First tests of a centrifugal particle receiver with a 1m2 aperture," in *SolarPACES*, Santiago, Chile, September 26 - 29 2017, vol. 2033, no. 040004: AIP Conference Proceedings, doi: https://doi.org/10.1063/1.5067040.

[12] M. Ebert, L. Amsbeck, J. Rheinländer, B. Schlögl Knothe, S. Schmitz, M. Sibum, R. Uhlig, R. Buck,, "Operational experience of a centrifugal particle receiver prototype," in *SolarPACES*, Casablanca, Morocco, October 1-4 2018, vol. 2126, no. 030018: AIP Conference Proceedings, pp. 1-8, doi: https://doi.org/10.1063/1.5117530.

[13] M. Ebert, L. Amsbeck, R. Buck, J. Rheinländer, B. Schloegl-Knothe, S. Schmitz, M. Sibum, H. Stadler, R. Uhlig, "First on-sun tests of a centrifugal particle receiver system," in *Proceedings of the ASME 2018 Power and Energy Conference PowerEnergy* Lake Buena Vista, Florida, USA, June 24–28 2018, no. V001T11A002: ASME, doi: https://doi.org/10.1115/ES2018-7166.

[14] S. Hicdurmaz, E. Johnson, J. Grobbel, L. Amsbeck, R. Buck, and B. Hoffschmidt, "Numerical Heat Transfer Modelling of a Centrifugal Solar Particle Receiver," in *SolarPACES*, Virtual Conference, September 28 - October 2, 2020 2020: AIP Conference Proceedings, doi: https://doi.org/10.1063/5.0086375.

[15] M.F. Modest, Radiative Heat Transfer, 2nd ed., Academic Press, 2003, p. 269.

[16] J. Chen, A. Kumar, J. Coventry, J. Kim, W. Lipinski, Numerical modelling of radiative heat transfer in a polydispersion of ceramic particles under direct high-flux solar irradiation, Journal of Quantitative Spectroscopy & Radiative Transfer 278 (2022) 108008, https://doi.org/10.1016/j.jqsrt.2021.108008.

[17] L. Hespel, S. Mainguy, J. Greffet, Radiative properties of scattering and absorbing dense media: theory and experimental study, Journal of Quantitative Spectroscopy & Radiative Transfer 77 (2003) 193–210, https://doi.org/10.1016/S0022-4073(02)00123-1.

[18] R. Jiang, M. Li, W. Wang, X. Xue, D. Li, A new methodology of thermal performance improvement and numerical analysis of free-falling particle receiver, Solar Energy 230 (2021) 1141–1155, https://doi.org/10.1016/j.solener.2021.11.043.

[19] N.P. Siegel, C.K. Ho, S.S. Khalsa, G.J. Kolb, Development and evaluation of a prototype solid particle receiver: on-sun testing and model validation, J. Solar Energy Engineering 132 (2) (2010) 021008, https://doi.org/10.1115/1.4001146.

[20] S.N. Kostenkov, E.V. Kharanzhevskii, M.D. Krivilev, Determination of characteristics of laser radiation interaction with nanocomposite powder materials, The Physics of Metals and Metallography 113 (2012) 98–103, https://doi.org/10.1134/S0031918X12010061.

[21] A. Streek, P. Regenfuss, H. Exner, Fundamentals of Energy Conversion and Dissipation in Powder Layers during Laser Micro Sintering, in: Lasers in Manufacturing Conference 2013, vol. 41, Physics Procedia, 2013, pp. 858–869, https://doi.org/10.1016/j.phpro.2013.03.159.

[22] A.V. Gusarov, Radiative transfer, absorption, and reflection by metal powder beds in laser powder bed processing, Journal of Quantitative Spectroscopy & Radiative Transfer 257 (107366) (2020) pp, https://doi.org/10.1016/j.jqsrt.2020.107366.

[23] O.B. Kovalev, A.V. Gusarov, V.V. Belyaev, Morphology of random packing of micro-particles and its effect on the absorption of laser radiation during selective melting of powders, International Journal of Engineering Science 157 (103378) (2020) pp, https://doi.org/10.1016/j.ijengsci.2020.103378.

[24] E.F. Johnson, S. Hicdurmaz, R. Buck, B. Hoffschmidt, Beam radiation penetration in particle beds for heat transfer modeling of a centrifugal solar particle receiver, Journal of Quantitative Spectroscopy and Radiative Transfer 295 (108403) (2022) pp, https://doi.org/10.1016/j.jqsrt.2022.108403.

[25] S. Hicdurmaz, J. Grobbel, R. Buck, and B. Hoffschmidt, "A numerical radiation model for the centrifugal particle solar receiver," in *SolarPACES 2021*, Virtual, Online, September 27 – October 1 2021, vol. 2815: AIP Conference Proceedings pp. 100005 (1-9), doi: https://doi.org/10.1063/5.0148791.

[26] E.F. Johnson, I. Tarı, D. Baker, Radiative heat transfer in the discrete element method using distance based approximations, Powder Technology 380 (2021) 164–182, https://doi.org/10.1016/j.powtec.2020.11.050.

[27] S.Y. Jeong, C. Chen, D. Ranjan, P.G. Loutzenhiser, Z.M. Zhang, Measurements of scattering and absorption properties of submillimeter bauxite and silica particles, Journal of Quantitative Spectroscopy & Radiative Transfer 276 (2021) 107923, https://doi.org/10.1016/j.jqsrt.2021.107923.

[28] F. Sutter, M. Montecchi, A. M. Sabio, G. S. Vicente, A. Fernández-García, et. al., "Round Robin Test of Absorptance and Emittance of Particles for CSP," in *26th SolarPACES Conference*, Albuquerque, USA, 2022: AIP Conference Proceedings.

[29] N.P. Siegel, M.D. Gross, R. Coury, The development of direct absorption and storage media for falling particle solar central receivers, Journal of Solar Energy Engineering vol. 137, no. 4(041003) (2015), https://doi.org/10.1115/1.4030069.

[30] E.F. Johnson, İ. Tarı, D. Baker, A monte carlo method to solve for radiative effective thermal conductivity for particle beds of various solid fractions and emissivities, Journal of Quantitative Spectroscopy and Radiative Transfer 250 (107014) (2020) pp, https://doi.org/10.1016/j.jqsrt.2020.107014.

[31] E. F. Johnson. "https://github.com/ef-johnson/Radiation-Penetration-Depth-in-Particle-Beds." (accessed 02 February 2022, 2022).

[32] Z.M. Zhang, Nano/Microscale Heat Transfer, 2nd ed., Springer, 2020, pp. 448–449.

[33] F.E. Nicodemus, J.C. Richmond, J.J. Hsia, I.W. Ginsberg, T. Limperis, Geometrical Considerations and Nomenclature for Reflectance, United States. Government Printing Office, Washington D.C., 1977.

[34] J. Grobbel, Modeling Solar Particle Receivers with the Discrete Element Method, RWTH Aachen University, Aachen, Germany, 2019. Ph.D. Thesis.

[35] S. Hicdurmaz, R. Buck, and B. Hoffschmidt, "Discrete Element Method Modelling of the Particle Flow in Centrifugal Solar Particle Receiver," in *SolarPACES 2022*, New Mexico, USA, 2022: TIB Open Publishing (In Press).